Available online at www.sciencedirect.com

SCIENCE DIRECT®

Earth and Planetary Science Letters 234 (2005) 207–221

EPSL

www.elsevier.com/locate/epsl

Basaltic volcanism and mass extinction at the Permo-Triassic boundary: Environmental impact and modeling of the global carbon cycle

A. Grard[a], L.M. François[a,c,*], C. Dessert[b,d], B. Dupré[b], Y. Goddéris[b]

[a]*Laboratoire de Physique Atmosphérique et Planétaire, Université de Liège, Bât. B5c, 17 Allée du Six Août, B-4000 Liège, Belgium*
[b]*Laboratoire des Mécanismes de Transfert en Géologie, UMR 5563, CNRS-Université Paul Sabatier-IRD, Toulouse, France*
[c]*Centre de Recherches Pétrographiques et Géochimiques, CNRS, Vandoeuvre-lès-Nancy, France*
[d]*Department of Earth Sciences, University of Cambridge, Cambridge, UK*

Received 12 October 2004; received in revised form 26 January 2005; accepted 10 February 2005
Available online 26 April 2005
Editor: V. Courtillot

Abstract

The Siberian Traps represent one of the most voluminous continental flood basalt provinces on Earth. The mass extinction at the end of the Permian was the most severe in the history of life. In the present paper, these two major concurrent events that occurred are analysed and a geochemical model coupled with an energy balance model is used to calculate their environmental impact on atmospheric CO_2, oceanic $\delta^{13}C$, and marine anoxia. The latitudinal temperature gradient is reduced relative to today, resulting in warmer temperatures at high latitudes. The warmer climate and the presence of fresh basaltic provinces increase the weatherability of the continental surfaces, resulting in an enhanced consumption of atmospheric CO_2 through weathering. First, the eruption of the Siberian traps is accompanied by a massive volume of ^{13}C depleted CO_2 degassed from the mantle and added to the ocean through silicate weathering, thus lowering marine $\delta^{13}C$. Second, the rapid collapse in productivity induces a strong decrease in the global organic carbon burial. This too tends to increase the proportion of light carbon in the ocean. These two effects can explain the low $\delta^{13}C$ values across the PT boundary, and methane release need not be invoked to explain the $\delta^{13}C$ fluctuations. It is proposed that the phosphorus cycle, which drives primary production in the model, plays an important role on the recovery of productivity and the $\delta^{13}C$ variations.

Keywords: Permo-Triassic boundary; carbon cycle; basaltic traps; extinction; modeling

1. Introduction

During the Late Permian, about 250 million years ago (Ma), the continents were aggregated into the supercontinent Pangea. The breakup of Pangea began

* Corresponding author. Tel.: +32 4 366 97 76; fax: +32 4 366 97 11.
E-mail address: francois@astro.ulg.ac.be (L.M. François).

0012-821X/$ - see front matter © 2005 Elsevier B.V. All rights reserved.
doi:10.1016/j.epsl.2005.02.027

shortly after the emplacement of basaltic traps, which now cover vast areas of the Siberian platform. The original volume of basalt exceeded 2×10^6 km^3, and may have reached twice that amount [1], but only 4×10^5 km^3 currently remain. Kerrick [2] estimated a total volume of about 3.3×10^6 km^3, but many authors [3,4] assume that the area of the basaltic flows was about 1.5×10^6 km^2, although the present-day area of basalts is much smaller (3.4×10^5 km^2). According to Reichow et al. [5], the total area of the traps is at least doubled (and possibly more than tripled) by inclusion of the West Siberian Basin (WSB) basalts, giving a combined area of 3.9×10^6 km^2 and making the Siberian flood basalt province the largest subaerial volcanic event in the Phanerozoic record. Claoué-Long et al. [6] obtained U–Pb dates of zircons from an ash band immediately below the PT boundary in Southern China of 251.2 ± 3.4 Ma. Renne et al. [7] analysed sanidine from the same ash band and obtained an ^{40}Ar–^{39}Ar age of 249.91 ± 1.52 Ma. Redating the same ash band again, Bowring et al. [8] obtained a U–Pb age of 251.4 ± 0.3 Ma. These dates suggest the PT boundary occurred between 250 and 251 Ma, with a greater likelihood for the older end of this age range. More recently, Mundil et al. [9] concluded that the PT boundary must be slightly older than 252.5 ± 0.3 Ma. The radiometric dating efforts suggest that the onset of eruptions was coincident with the PT boundary within a few hundreds of thousands of years. Estimates for the duration of volcanism range from 0.6 [10] to 1 million years [7].

During the end Permian mass extinction, it is estimated that 96% of marine species [11] and 70% of terrestrial vertebrate families went extinct [7]. Land plants were also affected. The causes of this catastrophic event are currently a topic of intense debate. Many processes have been offered to explain the biological extinction, including changes in sea level, climate change, large-scale volcanism, overturn of the ocean with the release of toxic gases, massive methane release from methane hydrates, a bolide impact, and others [12]. However, confusion remains in regard to whether geochemical signatures at the PT boundary reflect the causes or the effects of the extinction. For example, the release of isotopically light carbon into the atmosphere by volcanism induces a drop in the carbon isotopic composition (δ^{13}C) of the oceans, but this drop could also have been generated by a sudden mass extinction. In any case, given the coincidence between Siberian Trap emplacement and the PT boundary, it seems likely that volcanism at least contributed to the extinction [1,7,8].

Jin et al. [13] suggest that the peak in extinction rates occurred at 251.4 Ma, followed by the gradual disappearance of a small number of surviving genera over the next million years. The rapid marine extinction in the Meishan sections of Southern China coincides with the dramatic shift in the δ^{13}C composition of seawater (Fig. 1). According to Bowring et al. [8], the age of the event boundary is also 251.4 ± 0.3 Ma at Meishan, and the biostratigraphically defined PT boundary is $< 251.4 \pm 0.3$ Ma and $> 250.7 \pm 0.3$ Ma. Their geochronological data indicate that the main pulse of Changhsingian

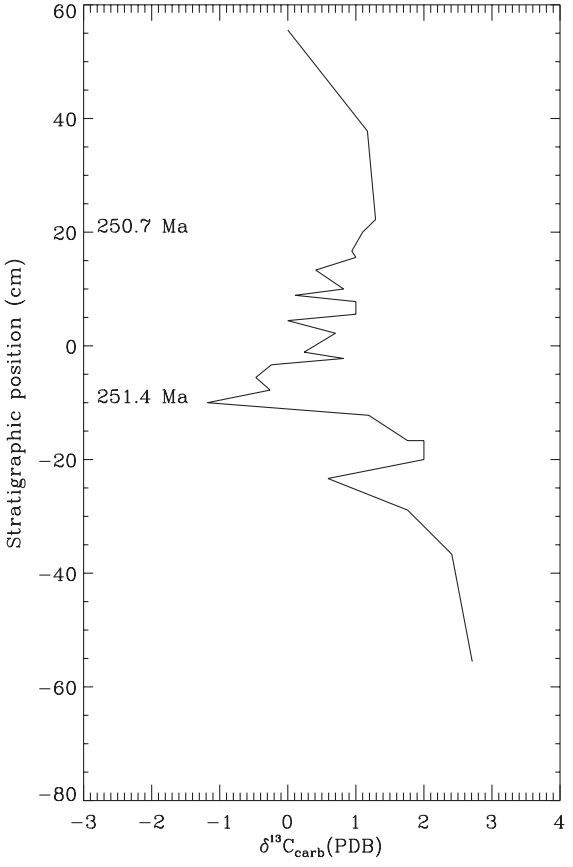

Fig. 1. Carbon isotope profile of PT boundary interval at section B of Meishan, China. Horizontal scale is δ^{13}C in ‰; numbers on the right-hand side are ages in million years. After Jin et al. [13].

extinction occurred in less than 1 million years (my), between 251.4 ± 0.3 and 252.3 ± 0.3 Ma. At Meishan, as well as at the other sections, there are abrupt negative shifts in the $\delta^{13}C$ value of both inorganic and organic carbon at the PT boundary [14,15]. The amplitude and duration of the shifts are a function of accumulation rate and sampling interval. In many studies, a shift from the Late Permian to the Early Triassic values of − 2‰ to − 4‰ is observed, with the maximum excursion approximately coincident with the boundary [16]. Holser et al. [17] suggest a duration for the extinction of 5–10 my, whereas Hallam and Wignall [18] prefer a 'rapid but not instantaneous' mass extinction. The knowledge of sediment accumulation rates at particular locations is needed to assign an actual duration to the extinction. Bowring et al. [8] obtained ages at Meishan that differed by 0.7 ± 0.3 my for two ash layers that bracket the extinction period. Twitchett et al. [19] suggest a more rapid rate of ecosystems collapse of 10–30 thousand years for the marine extinctions based on typical sediment accumulation rates.

Marine sediments deposited in the latest Permian record a change from oxic to anoxic conditions. This transition period is marked by the development of widely distributed facies, consisting of variable proportions of thinly bedded marls, micritic limestones [20] and sediments rich in organic matter (e.g. black shales) [21]. The abundance of pyrite (FeS_2) and fine lamination implies that the rocks were deposited in a low-oxygen environment. Global warming contributes to lower oxygen concentrations in two ways [22]: (1) oxygen uptake by organisms increases rapidly with a rise in temperature, and (2) oxygen solubility in seawater decreases with an increase in temperature. Yet, the single most important cause of oxygen deficiency in bottom waters was likely a decline in the intensity of ocean circulation resulting from a decline in equator-to-pole temperature gradient [22]. An ocean depleted in oxygen is clearly an unfavourable environment for most animals, and anoxic waters are a plausible killing mechanism.

Volcanic emissions can affect climate on different timescales [23]. Volcanoes release gases into the stratosphere: SO_2 which is rapidly oxidised to yield sulfate aerosols producing short-term cooling (sulfate aerosols scatter the solar radiation back into space and, in the lower atmosphere, they can nucleate water droplets and modify the radiative properties of clouds; they are, however, removed from the atmosphere after 1 to 2 years), and CO_2 which generates long-term warming.

In this paper, we explore the impact of the emplacement of the Siberian traps on the global carbon cycle, on the mass extinction, and the subsequent weathering of this large basaltic province. We also try to explain how these events have modified the $\delta^{13}C$ record across the PT boundary.

2. Weathering of continental flood basalts

Volcanic eruptions are known to have short-term effects on global climate through the release of aerosols to the stratosphere. Large volcanic eruptions are thus potential candidates for initiating major climatic and biological crisis in the Earth's history. In contrast, tectonic activity and average volcanism are generally regarded as one of the major driving forces of climate change on geological timescales (> 1 my) due to the release of CO_2 into the atmosphere and the associated greenhouse warming. On these timescales, the volcanic release of CO_2 into the atmosphere–ocean system is counterbalanced by its consumption during silicate weathering and subsequent carbonate deposition [24]. This balance is maintained dynamically via the negative feedback of silicate weathering, as the system evolves towards hypothetical steady state. Hence, chemical silicate weathering plays a major role in the long-term evolution of atmospheric CO_2 partial pressure.

Dessert et al. [25] have quantified the impact of the emplacement of the K/T Deccan traps on the global carbon cycle and climate. The weathering rate of continental silicates, including the flood basalts, is enhanced under a warmer and wetter climate [26], and this stabilizes the partial pressure of atmospheric CO_2, increasing the sink as the source increases. Atmospheric CO_2 thus reaches a new steady state several million years after the end of trap emplacement and degassing. Because basaltic rocks weather about 5 to 10 times faster than granitic rocks [27], the global weatherability of the continental surface drastically increases after the eruption of large continental flood basalts, and the new steady state atmospheric CO_2 and

mean global air temperature drop below the pre-perturbation values.

The original volume of the Siberian flood basalts may have reached 3×10^6 km^3, which corresponds to a total degassing of 1.6×10^{18} mol of CO_2 (equivalent to the Deccan traps degassing [28]). Continental reconstructions for the end of the Permian (e.g. [29]) indicate that the Siberian platform was located between 60° and 70°N at the time of trap emplacement and has not moved substantially in latitude since. The current climate is cold and dry in these latitudes, and the weathering of the Siberian traps is weak. But in the past, the weathering of these basalts may have had a major impact on the atmospheric CO_2 and climate, particularly towards the end of the Paleozoic when the high latitudes were warmer than today [30].

The massive subaerial intracontinental volcanism, combined with a voluminous subduction-related volcanism along the Proto-Cordilleran–Gondwana and Proto-Altaid orogens [31], presumably caused an increase in atmospheric CO_2 partial pressure. However, the aerosol-induced reduction in solar irradiation and the enhanced consumption of atmospheric CO_2 by continental silicate weathering of the newly exposed basaltic surface more than compensated for this 'greenhouse' effect.

3. Model considerations

In this contribution we quantify the events at the PT boundary with a numerical model that incorporates the biogeochemical carbon and alkalinity cycles. We calculate the long-term changes in atmospheric CO_2 concentrations and the geochemical signatures of elements across the transition boundaries. The three-box model (atmosphere, surface and deep ocean) in this study describes the global organic and inorganic carbon and alkalinity cycles. Time-dependent mass balance equations are written for total carbon, alkalinity, phosphorus, oxygen (O_2), and ^{13}C. The temporal evolution of the following fluxes is calculated: atmosphere–ocean exchange, weathering of silicates, weathering and precipitation of carbonates, weathering of kerogen carbon and deposition of organic carbon (Fig. 2). This geochemical model is coupled to a 1D energy balance model (EBM) that calculates annual mean air temperature as a function of atmospheric CO_2 pressure in 18 latitude bands [32], with the continental zonal runoff calculated as a parametric function of the zonal air temperature, continental area and latitude. In the Late Permian, the latitudinal temperature gradient was reduced compared to today (~20 °C) [30]; therefore we force the model to flatten the gradient, which makes the high latitudes warmer. As a result, the heat transfer coefficients D_s (sensible heat), D_l (latent heat), and D_o (oceanic heat), which are assumed to vary with latitude, are doubled. We adopt a Late Permian paleogeography [33] and a solar luminosity reduced by 2% relative to the present [34,35]. The main outputs of the model are the mean $\delta^{13}C$ evolution of marine dissolved inorganic carbon, atmospheric pCO_2, alkalinity and carbon contents of the oceans, and a plethora of carbon and alkalinity exchange fluxes between the exosphere and sedimentary reservoirs.

The quantification of the effects of basaltic trap emplacement on silicate weathering rates requires global weathering laws. The calculations use the temperature output from the EBM where temperature-dependent weathering rates are assumed. Runoff and weathering rates are calculated for each latitude band. Four lithologies are considered: basalts, other silicates rocks (granites, gneisses), carbonates and shales (sedimentary rocks rich in organic matter). A different weathering law is used for each lithology and latitude band. The consumption of atmospheric CO_2 by the weathering of basalts (noted b) and other silicates rocks (noted g) can be written as:

$$f_{w,i}^{g,b} = \text{area}_i^{g,b} \cdot \text{runoff}_i \cdot k^{g,b} \cdot \exp\left(C^{g,b} \cdot \text{WT}\right) \quad (1)$$

Area_i^g and area_i^b represent the continental area (in square kilometres) of exposed granitic and basaltic surfaces in latitude band i. Runoff_i is the continental runoff in mm/year within a given latitude band i. k^g and k^b are constant for granite and basalt, respectively, and are calibrated in such a way that for present-day climatic and paleogeographic conditions $F_w^g + F_w^b = F_w^{sil}$ (global silicate weathering flux) equals 5.85×10^{12} mol/year [36]. F_w^b is adjusted to be approximately the value used by Dessert et al. [27], and F_w^g is calibrated by difference (Table 1). The CO_2 consumption flux due to the weathering of the

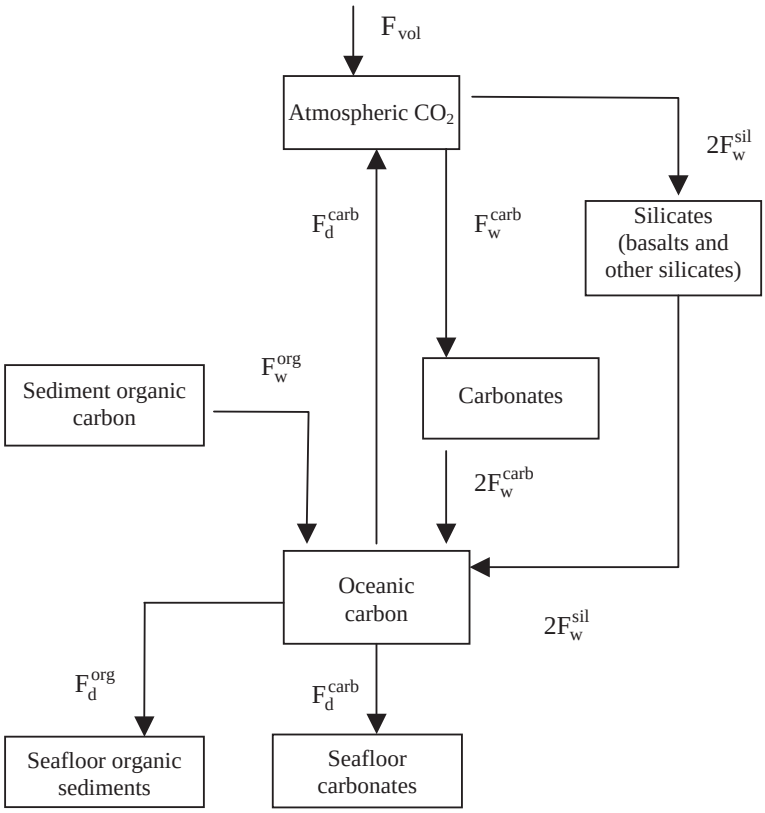

Fig. 2. Schematic diagram illustrating the carbon and alkalinity fluxes considered in the model. F_{vol} is the flux of volcanic CO_2; F_w^{sil} is the uptake of atmospheric CO_2 by weathering of silicates and transfer of carbon into the oceans; F_w^{carb} is the uptake of atmospheric CO_2 by weathering of carbonates (the flux of carbon to the oceans from carbonate weathering is twice this value); F_w^{org} is the weathering flux of sedimentary organic carbon; F_d^{carb} is the burial flux of marine carbonates (equal at steady state to the net flux $F_{oa}-F_{ao}$ of CO_2 from ocean to the atmosphere); F_d^{org} is the burial flux of organic carbon in sediments. After Beerling and Berner [61].

Siberian traps is estimated to be 0.053×10^{12} mol/year [27]. C^g and C^b are constants representing the temperature dependence of the weathering rate for each lithology. WT is the average air temperature in °C during the weathering season, i.e. the time period with temperatures higher than a threshold T_0 (=0 °C). WT is parameterized as a function of the annual mean temperature calculated by the EBM in the latitude band i:

Table 1
Main parameters of the geochemical model

Parameter	Value	Reference
Age of the Siberian traps	251.4 Ma	[8]
Area of the Siberian traps	2.5×10^6 km^2	[3,4]
Present-day CO_2 consumption flux by carbonate weathering	12.3×10^{12} mol/year	[36]
Present-day CO_2 consumption flux by silicate weathering	11.7×10^{12} mol/year	[36]
Present-day CO_2 consumption flux by basalt weathering	3.11×10^{12} mol/year	[27]
CO_2 release from Siberian traps pulses	1.6×10^{18} mol	[28]
Age of the mass extinction	251.4 Ma	[13]

$$\text{if } 252.16\text{ K}<T_i\leq 294.88\text{ K},\quad \mathrm{WT}=10.6783+0.508691\cdot(T_i-273.15) \tag{2}$$

$$\text{if } 250.95\text{ K}\leq T_i\leq 252.16\text{ K},\quad \mathrm{WT}=0 \tag{3}$$

$$\text{if } T_i\geq 294.88\text{ K},\quad \mathrm{WT}=T_i-273.15 \tag{4}$$

Note that, if $T_i<250.95$ K, $f_{w,i}^{g,b}=0$ and the global silicate weathering flux is also zero. New et al. [37] compiled a high-resolution data set of surface climate

over global land areas. Using the mean monthly surface temperature from these data, we calculate the mean annual temperature and plot it against the average monthly positive temperatures at each location. The correlation coefficient between the data set and the WT relation is about 0.98. Where there is no positive monthly temperature, there is no weathering season (WT=0). Where monthly temperatures are all positive, the weathering season lasts the entire year (WT=T). Simple linear scaling is used to interpolate between these two extremes. It should be noted that the threshold T_0 that determines the weathering season is not well known, and several tests using a lower threshold (−5 °C) showed no fundamental difference.

The carbonate weathering law ($f_{w,i}^{carb}$) is proportional to the continental surface covered by carbonates in each latitude band, the continental runoff, and the calcium ion concentration of the solution in equilibrium with both calcite and atmospheric CO_2.

The kerogen weathering law ($f_{w,i}^{org}$) is similar to that for basalt weathering, except that in this case there is no temperature dependence [38].

The pre-trap steady state can be controlled by the balance between CO_2 degassing sources and the silicate weathering flux ($F_w^{sil} = \sum_{i=1}^{18} f_{w,i}^{g} + \sum_{i=1}^{18} f_{w,i}^{b}$), that is the net carbon released into the ocean–atmosphere system is equal to the total consumption of carbon by continental silicate weathering. This implies that the organic carbon subcycle is also assumed to be in balance. After basalt spreads over a granitic lithology within a given latitude band, a new steady state is achieved by the global ocean–atmosphere carbon cycle within several million years.

A simple chemical model of phosphorus and oxygen cycling is included in the coupled model. The input flux of phosphorus is taken to be proportional to the continental silicate weathering flux. Two processes are taken into account as important phosphorus sinks [39], the burial of phosphorus tied up in organic matter and the sedimentation of calcium carbonates. Phosphorus is chosen as a driver of productivity because it is thought to exert the primary control on marine primary production on long timescales [40].

The organic carbon subcycle includes the burial of organic (reduced) carbon, C_{org}, and the oxidation of kerogen on continents. The kerogen weathering flux (F_w^{org}) was already described above. The depositional flux of organic matter (F_d^{org}) is proportional to the new productivity, which in turn depends on the phosphorus content. The organic carbon cycle likely modulated the isotopic evolution of the oceans [41], through disequilibria between kerogen carbon weathering and organic carbon deposition. Due to the large carbon isotopic fractionation in the organic carbon subcycle, the seawater $\delta^{13}C$ is directly related to the amplitude of the imbalance between F_d^{org} and F_w^{org}. We also investigate the isotopic effect on seawater of the massive release of mantle ^{13}C-depleted CO_2 ($\delta^{13}C_{vol}=-5‰$) to the atmosphere during eruption of the Siberian traps. The degassing of large quantities of mantle carbon also increases weathering through the effect of warming, resulting in increased CO_2 consumption and delivery of alkalinity and phosphorus to the ocean.

A series of differential equations is used to track the evolution of the $\delta^{13}C$ composition of the atmosphere (δ_a), the surface ocean (δ_s) and the deep ocean (δ_d) (see Table 2 for explanation of the variables).

· For the atmosphere:

$$\frac{d\delta_a}{dt} = \frac{F_{vol}\cdot(\delta_{vol}-\delta_a) + F_{oa}\cdot(\delta_g-\delta_a)}{C_a} \tag{5}$$

· For the surface ocean:

$$\begin{aligned}\frac{d\delta_s}{dt} = \Big[\Big[& F_{mix}\cdot(C_{od}/V_{od})\cdot(\delta_d-\delta_s) \\ & - \text{bionp}\cdot\text{rcp}\cdot\text{rcarb}\cdot(\delta CO_3-\delta_s) - \text{bionp}\cdot\text{rcp} \\ & \cdot(\delta_{org}-\delta_s) - F_{oa}\cdot(\delta_g-\delta_s) + F_{ao}\cdot(\delta_a-\delta_s) \\ & + (2F_w^{sil}+F_w^{carb})\cdot(\delta_a-\delta_s) + F_w^{carb}\cdot(\delta_{cw}-\delta_s) \\ & + F_w^{org}\cdot(\delta_{ow}-\delta_s)\Big]\Big/ C_s\Big]\end{aligned} \tag{6}$$

· For the deep ocean:

$$\begin{aligned}\frac{d\delta_d}{dt} = \Big[\Big[& F_{mix}\cdot(C_{os}/V_{os})\cdot(\delta_s-\delta_d) \\ & + (\text{bionp}\cdot\text{rcp}\cdot\text{rcarb} - F_d^{carb})\cdot(\delta CO_3-\delta_d) \\ & + (\text{bionp}\cdot\text{rcp} - F_d^{org})\cdot(\delta_{org}-\delta_d)\Big]\Big/ C_d\Big]\end{aligned} \tag{7}$$

Table 2
Description of variables from Eqs. (5)–(7) (Section 3)

Equations	Variables	Description
Eq. (5)	δ_a	atmospheric $\delta^{13}C$
	δ_{vol}	$\delta^{13}C$ of volcanic CO_2 (weighted average of contributions from MOR: mid-ocean ridge, continental margin volcanism, continental flood basalt)
	δ_g	$\delta^{13}C$ of gaseous CO_2 in the surface ocean (taking into account fractionation ε_{dg} between the gaseous and dissolved CO_2 [43])
	C_a	carbon content of the atmosphere
	F_{vol}	total volcanic CO_2 emission
	F_{oa}	exchange flux from the surface ocean to the atmosphere
Eq. (6)	δ_s	$\delta^{13}C$ value of the surface ocean
	δ_d	$\delta^{13}C$ value of the deep ocean
	δ_{CO_3}	$\delta^{13}C$ of the surface ocean CO_3^{-2} (taking into account fractionation ε_{bc} between bicarbonate and carbonate ions)
	δ_{ow}	$\delta^{13}C$ of the weathering flux of organic matter (−22‰)
	δ_{org}	$\delta^{13}C$ of the organic matter deposition flux taking into account the effect of isotopic fractionation due to photosynthesis ε_p [42]
	δ_{cw}	$\delta^{13}C$ of the weathered carbonated rocks
	C_{od}	carbon content of the deep oceanic reservoir
	C_s	carbon content of the surface ocean
	V_{od}	volume of the deep ocean
Eq. (7)	F_{mix}	mixing of waters between superficial and deep ocean reservoir
	F_{ao}	exchange flux from the atmosphere to the surface ocean
	F_w^{carb}	global carbonate weathering flux
	F_w^{org}	global organic matter weathering flux
	bionp	new biological productivity (in moles of phosphorus)
	rcp	Redfield ratio
	rcarb	$CaCO_3$ to organic carbon molar ratio in the biological production
	C_d	carbon content of the deep ocean
	C_{os}	carbon content of the surface oceanic reservoir
	V_{os}	volume of the surface ocean
	F_d^{carb}	global carbonate depositional flux
	F_d^{org}	global organic matter depositional flux

δ_s and δ_d represent the average $\delta^{13}C$ composition of dissolved inorganic carbon (DIC) in their respective reservoirs. From the carbonate equilibria, the model calculates the concentrations of H_2CO_3, HCO_3^- and CO_3^{2-} in the surface and deep ocean reservoirs, as well as their respective isotopic compositions $\delta_{H_2CO_3}$, δ_{HCO_3}, and δ_{CO_3}. The isotopic fractionation between the carbonate species and the isotopic fractionation due to photosynthesis are calculated as a function of temperature according to Freeman and Hayes [42], while the fractionation between dissolved and gaseous CO_2 is calculated according to Mook et al. [43].

The magnitude and global nature of the large negative excursions in carbon, sulfur and strontium isotopic compositions of surface waters [44], and anoxia led some authors [22,45,46] to propose that the entire ocean was severely stratified prior to the PT boundary, and that stagnation-induced anoxia may have played a role in the extinction at the end of the Permian. In this scenario, the marine extinction mechanism would have been closely related to the development of oxygen-deficient depositional environments. In the model, the oxygen concentration is calculated for the atmosphere, and the surface ocean is assumed to be in equilibrium with the atmosphere. The oxygen exchange between the surface and deep ocean is calculated to test whether or not the model can impose deep ocean anoxia.

4. Results

Environmental conditions (solar luminosity, land area, degassing rate, latitudinal distribution of lithologies), fluxes and reservoir sizes prior to the perturbation event imposed on the model are those for the Late Permian. They are comparable to those used or calculated by the GEOCARB model [38] for the same period.

4.1. Standard simulation

In this subsection, we illustrate with the model the sequence of events subsequent to the extrusion of the Siberian basaltic province. The pre-perturbation pCO_2 is assumed to be the Permian level calculated by the model (3080 ppmv). The eruptive phase is assumed to last 600 thousands years (ky) [10], with a total degassing of 1.6×10^{18} mol of CO_2 [28], similar to the rates proposed by Berner [12] and Kamo et al. [47]. The baseline CO_2 degassing used in the model is taken from Engebretson et al. [48], and is therefore significantly less than the rate reconstructed by Gaffin [49]. The area of the basaltic floods, another critical

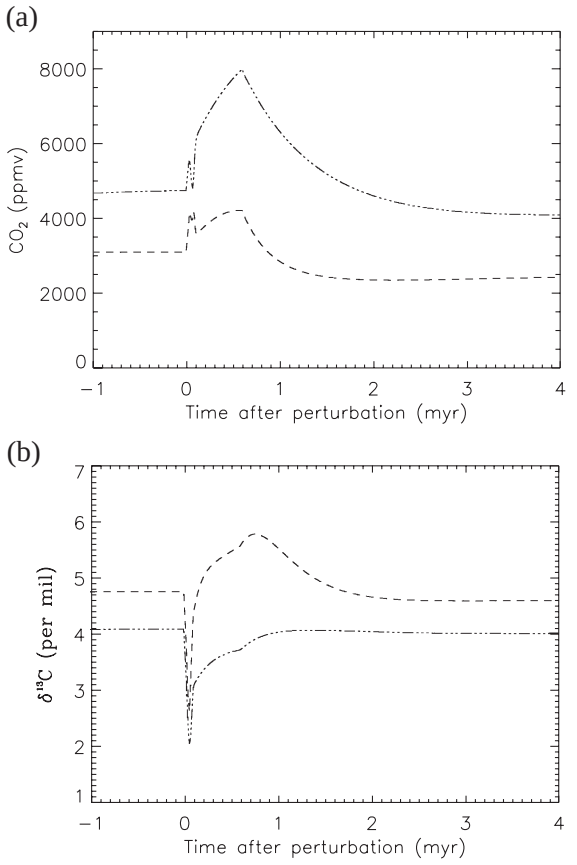

Fig. 3. Plots of atmospheric CO_2 and oceanic $\delta^{13}C$ versus time for the combined inputs of carbon to the atmosphere from mass extinction and from volcanic CO_2 degassing due to Siberian volcanism. The model incorporates an imbalance in the rates of burial and weathering of sedimentary organic matter. The dashed lines correspond to the standard simulation and the "dash dot dot" lines to simulation in which the phosphorus cycle is considered to be in steady state. (a) CO_2 and (b) $\delta^{13}C$.

parameter, is variably set to 2.5×10^6 km^2 to account for just the main Siberian traps, and the more extreme value of 3.9×10^6 km^2 [5], which includes buried basaltic sequences in the West Siberian Basin.

In the reference run, two time-dependent forcing functions are imposed to the system: the eruptive phase and the mass extinction. It is not clear whether these two events were simultaneous [7], or whether volcanism slightly pre-dated the extinction event [47]. In the simulation, both events start at the same time. The mass extinction has a duration of 100 ky and, in order to simulate the marine ecosystem collapse, the new production is reduced by 80% during this time interval. Fig. 3 illustrates the combined effects of Siberian trap volcanism and the mass extinction on the $\delta^{13}C$ of seawater and the CO_2 level of the atmosphere. The atmospheric CO_2 level rises by about 1080 ppmv at the peak value, and global mean air temperature rises by about 1.2 °C. Two causes explain these effects. First, the release of volcanic CO_2 into the atmosphere increases the atmospheric greenhouse, and the Earth becomes warmer. Second, the reduction of marine productivity induces a strong decrease in the deposition of organic carbon (Fig. 4), leading to an accumulation of carbon in the exospheric system and in the atmosphere. The CO_2 spike appearing just before 0.1 my (Fig. 3a) is linked to the mass extinction forcing function. The reduced primary production induces rapid fluctuations in the deposition of carbonate on the seafloor, and the alkalinity contents of surface and deep oceanic reservoirs increase significantly. The result is a disequilibrium between the alkalinity and carbon pumps, and the alkalinity transfer dominates the exchanges during the extinction phase. Subsequently, CO_2 is rapidly consumed by silicate weathering and the new steady state atmospheric CO_2 and mean global air temperature are finally lower than the corresponding pre-perturbation values. After 2.3 my, the atmospheric pCO_2 is lowered by 746 ppmv compared to its value before the perturbation. This CO_2 decrease is accompanied by global cooling of 1.07 °C. In the model, we took

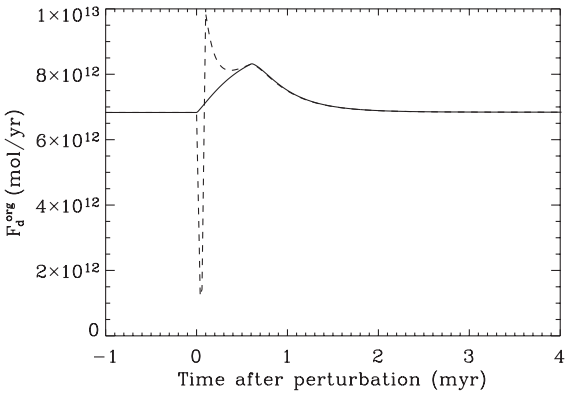

Fig. 4. Plots of the burial rate of sedimentary organic carbon (F_d^{org}) versus time at the PT boundary. The dashed line represents the standard simulation and the solid line the simulation in which only volcanic CO_2 released from the Siberian eruption is used to force the model.

into account changes in the areal extent of the basaltic province with time, as a result of erosion. The change in area is calculated using a linear relationship between the chemical weathering rate of basalts and CO_2 consumption that has previously been established for various basaltic catchments [27] and by approximating the geometry of the basalt province to be an inverted cone. We calculate that the Siberian traps province was reduced in area by a factor of two in 10 my, due to the warm and wet climate in the Late Permian and early Triassic. After this 10 my, the weathering rate was presumably reduced in response to high latitude cooling, except during the Eocene and the Cretaceous [50]. Consequently, the CO_2 consumption flux attributed to the basaltic weathering gradually decreases, and after 2.3 my, the atmospheric CO_2 level and global mean surface temperature increase slightly.

The rapid productivity collapse imposed on the system induces a strong decrease in organic carbon deposition, greatly decreasing the organic carbon burial sink for phosphorus. Since the source flux of phosphorus is proportional to the continental silicate weathering flux, the input of phosphorus to the ocean is enhanced throughout the 600 ky of Siberian volcanism. Therefore, phosphorus accumulates in the ocean, triggering a productivity bloom when photoautotrophs recover from the extinction event. The sharp rise in primary productivity increases the depositional flux of organic carbon, thus increasing the $\delta^{13}C$ of the ocean ($\delta^{13}C_{org} = -22‰$) and the oxygen production from the biosphere. However, oxygen consumption by heterotrophs is also stimulated, resulting in the development of anoxia in deep waters (Fig. 5). The high primary productivity is sustained by the elevated CO_2 flux from Siberian eruptions and consequent elevated silicate weathering flux that increases the phosphorus delivery to the ocean. The productivity bloom persists > 1 my and induces deep ocean anoxia for almost 0.9 my. Thus, the productivity crash is followed by productivity bloom, a pattern characteristic of oceans where a rapid decline in circulation rates produces an anoxic lower water column [22]. The carbon and phosphorus cycles are linked by the C/P ratio in the buried organic matter, which is a function of the degree of anoxicity of oceanic waters [51]. For simplicity, the C/P molar ratio in the buried sediments is considered to be

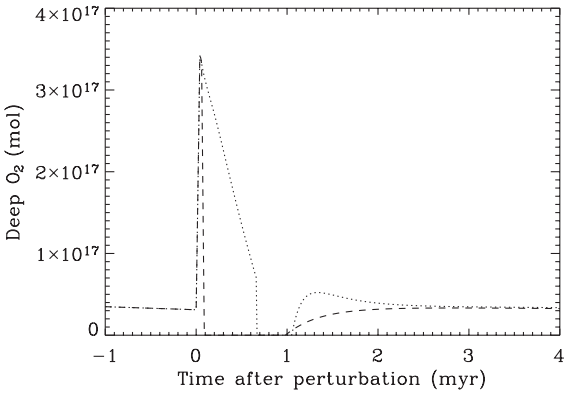

Fig. 5. Plots of deep marine oxygen concentration versus time at the PT boundary. The dashed line corresponds to the standard simulation and the dotted line to simulation where the mass extinction is protracted (0.7 my).

constant in the model. Modeling shows that the productivity declines concomitantly with the decrease in the rate of oceanic overturn and nutrient supply. This effect is counterbalanced by the increased availability of reactive phosphorus, which is not as efficiently sequestered by organic matter in an anoxic ocean. The result is a significant time lag (on the order of tens of ky) between the onset of oceanic anoxia and the build-up of phosphorus [22].

Mass mortality also affects marine plankton, and would virtually eliminate the biological pump, resulting in a decrease in the $\delta^{13}C$ composition of the surface ocean (i.e. a Strangelove Ocean [52]). D'Hondt et al. [53] have suggested a similar drop in $\delta^{13}C$ in the surface ocean during the K/T boundary interval.

The oceanic $\delta^{13}C$ values in the early and mid-Permian were high (+5‰, [12]), and remained elevated up to the PT boundary [44,54], where they dropped by 2‰ to 6‰. Either of the two forcing functions in our model can cause a decline in oceanic $\delta^{13}C$. First, volcanism could generate the anomaly, since mantle carbon is depleted in ^{13}C ($\delta^{13}C = -5‰$). Second, a decline in primary productivity would decrease the amount of ^{13}C-depleted organic carbon removed from the ocean. In our model, marine $\delta^{13}C$ falls by ~2.2‰ (Fig. 3b) at the PT boundary through a combination of these two effects. The negative excursion lasts ~140 ky and is followed by a positive excursion of ~1‰, which results from the accumulation of phosphorus in the ocean during the mass extinction.

4.2. Sensitivity tests

The organic carbon subcycle is badly constrained and we want to examine the role of organic matter weathering and deposition in the model. We also want to test the impact of the duration of mass extinction and the effect of the eruption alone without a contemporaneous mass extinction.

4.2.1. Organic carbon subcycle

In the reference run, the areal extent of the four model rock types is calculated for each latitudinal band from a simplified geological map published by UNESCO [55], a lithological map in Amiotte-Suchet et al. [56], and from other geological maps [23,57,58]. The weathering of silicate rocks is strongly dependent on climatic conditions (temperature and runoff) and constitutes a sink for atmospheric CO_2 that could strongly influence the partial pressure of CO_2. The latitudinal distribution of silicate rocks thus has an important impact on global climate. In order to test the impact of organic-rich rocks on the CO_2 sink, we prescribed them to be equally distributed in each latitude band. This reorganization of lithologies results in no significant impact on the weathering and burial fluxes of organic carbon, since kerogen weathering law in the model is not dependent on temperature.

4.2.2. Phosphorus subcycle

The burial flux of organic matter is proportional to the new productivity, which itself is dependent on phosphorus availability in the ocean. If the phosphorus cycle is in steady state (Fig. 3), the input flux to the ocean is independent of the continental silicate weathering flux. Similarly, the phosphorus burial flux is independent of the carbonate and organic carbon burial fluxes. Therefore, phosphorus does not accumulate in the ocean during the phase of enhanced silicate weathering, and there is no productivity bloom accompanying the primary production recovery. The organic carbon deposition remains constant in the simulation, except during the mass extinction, where it decreases by more than 85%. The well-balanced phosphorus cycle induces an important organic disequilibrium which increases the steady state atmospheric CO_2 pressure by 1650 ppmv (Fig. 3a). The elimination of the productivity bloom following the extinction removes the $\delta^{13}C$ positive excursion which was produced by the enhanced burial of organic carbon, but the amplitude of the negative $\delta^{13}C$ excursion is hardly affected (Fig. 3b).

4.2.3. Siberian volcanism

In the reference run, Siberian volcanism and mass extinction have been introduced in the model as coupled forcing functions. Here, we try to evaluate the impact of the eruption alone (Fig. 6). The primary production is driven by the phosphorus content of the ocean. The increase in the weathering input of phosphorus to the ocean during the enhanced silicate weathering period induces a rise

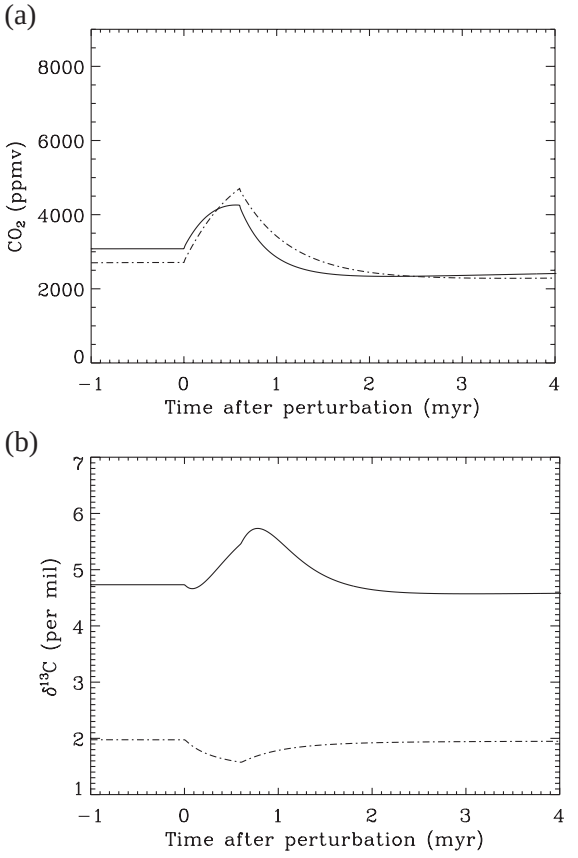

Fig. 6. Plots of atmospheric CO_2 and oceanic $\delta^{13}C$ versus time. Volcanic CO_2 release from the Siberian eruption is the only forcing function imposed on the model. The solid line simulates the Siberian volcanism event and the "dash dot" lines the same volcanism but without organic carbon and phosphorus cycling. (a) CO_2 and (b) $\delta^{13}C$.

by about 20% in marine production. However, without the productivity crash there is no significant accumulation of phosphorus in the ocean and thus no productivity bloom. The organic matter deposition is dependent on the new productivity and shows an increase of only about 1.5×10^{12} mol/year (Fig. 4). The enhanced organic burial flux counterbalances the effect on $\delta^{13}C$ of the input of ^{13}C-depleted volcanic carbon ($\delta^{13}C_{vol}=-5‰$). The drop in $\delta^{13}C$ is almost totally suppressed and only the positive excursion remains (Fig. 6b). The increase in marine primary production induces deep water anoxia which lasts about 0.77 my. The phosphorus cycle, and to a lesser extent the organic carbon cycle, mask the effect of volcanic CO_2 release on the $\delta^{13}C$ drop. In order to quantify this effect, we must remove the organic carbon and phosphorus cycling. Under these conditions, the steady state $\delta^{13}C$ is lower than in the reference run and the $\delta^{13}C$ negative excursion, due to the degassing of 1.6×10^{18} mol of mantle CO_2, is close to 0.4‰ (Fig. 6b). The drop in $\delta^{13}C$ is small and the volcanic degassing alone is clearly insufficient to explain the PT changes in $\delta^{13}C$.

A critical parameter in the model is the areal extent of the Siberian flood basalts. We have used the average value of 2.5×10^{6} km^2 [3,4], rather than the higher value of 3.9×10^{6} km^2 proposed by Reichow et al. [5]. A sensitivity test using the latter value results in greater consumption of atmospheric CO_2 due to weathering of silicates lithologies. The new steady state atmospheric CO_2 and mean global air temperature, following emplacement of the traps and subsequent weathering, are lower than in the reference run by 988 ppmv and 1.5 °C, respectively.

4.2.4. Duration of mass extinction

The amplitude of the $\delta^{13}C$ negative excursion at the PT boundary is about 3‰ (Fig. 1). Bowring et al. [8] estimated a duration of 0.7 ± 0.3 my for the mass extinction. If the primary production is strongly reduced (by about 80%) for a period of 0.7 my (compared to 0.1 my), the model produces a $\delta^{13}C$ drop of 3.3‰ (Fig. 7), which is a larger decline than produced in the reference run due to the greater imbalance between organic burial and organic weathering at the PT boundary. This

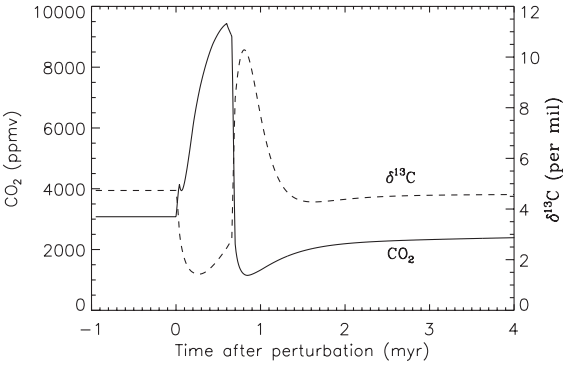

Fig. 7. Plots of atmospheric CO_2 and oceanic $\delta^{13}C$ versus time for the combined carbon input to the atmosphere from volcanic CO_2 degassing and from a long mass mortality period (0.7 my). The solid line represents the atmospheric CO_2 level and the dashed lines the $\delta^{13}C$ evolution.

situation results in a stronger concomitant rise of atmospheric CO_2 pressure of about 6300 ppmv (Fig. 7). The loss of productivity lasts longer than the Siberian volcanism. The perturbations of the carbon cycle linked to such a long ecosystem collapse are severe and result in a high atmospheric CO_2 pressure, high weathering fluxes and a large drop in $\delta^{13}C$. The total amount of phosphorus accumulated in the deep water reservoir during the low productivity phase is about 6 times higher than in the reference simulation. As a result, the productivity bloom following the extinction is much higher leading to pronounced deep water anoxia and to very high sedimentation rates of organic matter. The result is a very rapid drop of atmospheric CO_2 near 0.7 my when productivity recovers (Fig. 7). This CO_2 drop induces a strong reduction in the weathering rates and, hence, in the delivery of phosphorus to the ocean. Under low weathering rates and high organic matter sedimentation, the phosphorus cycle is largely out of balance and the deep ocean phosphorus content is reduced to its pre-perturbation value in a few hundreds of ky. Hence, the high productivity phase and the deep water anoxia are maintained for only 0.4 my (Fig. 5), a much shorter interval than in the standard simulation. Consequently, the productivity bloom and associated anoxia are driven essentially by the characteristics of the extinction imposed on the system. The Siberian traps volcanism, combined with the sudden mass mortality, could explain the negative excursion

in $\delta^{13}C$ and the anoxia in deep waters observed at the PT boundary.

5. Discussion

During Late Permian, nearly all continents were assembled into the supercontinent, Pangea. This continental configuration limited the effect of the ocean on coastal areas [59]. Numerical experiments with a three-dimensional global ocean model with a low equator-to-pole temperature gradient [30] and linked to a biogeochemical model of phosphate and oxygen cycling, suggest that oceanic circulation would have been weak and anoxia would have been widespread during the Permian. Polar warming and tropical cooling cause anoxia throughout the deep ocean by decreasing the amount of dissolved oxygen in the regions of deep water formation and by increasing nutrient utilization. Our model generates a global surface ocean temperature of about 21.7 °C and a CO_2 level of 3080 ppmv prior to the PT mass extinction and Siberian flood basalt eruption. Imposing the present temperature gradient on the model yields average surface ocean temperatures ~3.4 °C colder and an atmospheric CO_2 level of only 1530 ppmv. Thus, the warmer climate in the Late Permian sets the stage for the enhanced global weathering fluxes that severely perturbs the global carbon cycle and generate the drop in $\delta^{13}C$ at the PT boundary.

The reorganization of the carbon cycle is the combined result of the Siberian flood basalt volcanism and the sudden mass extinction of marine biota. The sensitivity tests demonstrate the important role of the organic carbon subcycle on the sudden drop in marine $\delta^{13}C$ at the PT boundary. The seawater $\delta^{13}C$ composition is directly related to the amplitude of the imbalance between kerogen carbon weathering and organic carbon deposition [12]. Since the burial of organic matter depends on marine productivity, a prolonged Strangelove Ocean increases the organic disequilibrium and the amplitude of the $\delta^{13}C$ negative excursion. Disregard of the organic carbon cycle feedbacks thus precludes a good fit to the observed $\delta^{13}C$ data. Unfortunately, despite the huge amount of marine proxy data and numerical models, the organic cycle is still poorly constrained with respect to the exchange fluxes between the oceanic and crustal reservoirs. Nevertheless, the organic weathering and burial laws calibrated to present-day conditions provide reasonable results in our model.

The volcanic CO_2 released with the massive eruption of the Siberian traps cannot alone explain the large drop in $\delta^{13}C$ and the deep waters anoxia at the PT boundary. As Broecker and Peacock proposed [60], the perturbations to the Earth's ecosystems induced by the massive PT extinction can best explain the abrupt $\delta^{13}C$ decrease. The relative timing of the mass extinction and volcanism has an important impact on the duration of the anoxia event that follows. If the interval of low primary productivity exceeds the duration of flood basalt eruption, the recovery of marine productivity is more pronounced. The carbon cycle perturbations and the primary production following recover are controlled by the characteristics of the mass extinction. In the reference run, with rapid rates of ecosystem collapse, the high input of phosphorus to the ocean during Siberian volcanism sustains the recovery phase and associated anoxia for a longer period of time.

Several authors have invoked methane release to explain the oceanic drop in $\delta^{13}C$ [12,19]. Whereas the release of CH_4 to the atmosphere will cause the $\delta^{13}C$ value of the ocean to decrease, it will not add appreciable CO_2 to the atmosphere. Contrary to Berner [12], it appears that mass mortality and massive volcanism can generate in our model the $\delta^{13}C$ anomaly recorded at the PT boundary.

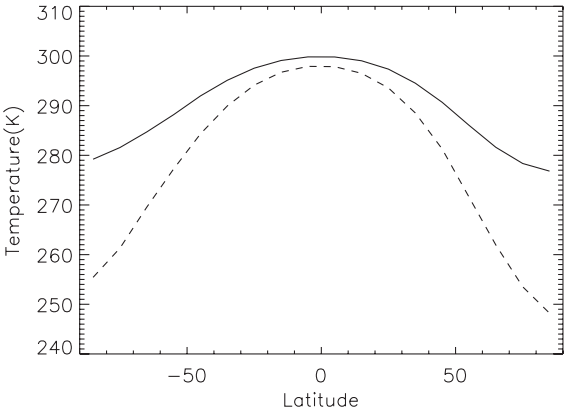

Fig. 8. Plots of latitudinal temperature gradient obtained from the 1D energy balance model. The solid line represents the latitudinal temperature gradient at the end of the Permian and the dashed line corresponds to the current one.

6. Conclusion

The Siberian traps are among the best-known flood basalt provinces. The latitudinal temperature gradient was reduced in the Permian compared to today (Fig. 8) and the high latitudes were wetter and warmer (281.6 K at the end of the Permian vs. 261.9 K today), which resulted in a relatively high rate of silicate weathering on the Pangean supercontinent.

A simple model to explain the geochemical and geological observations across the PT boundary includes a combination of causes: (1) the emplacement of the large basaltic province in Siberia, and (2) a severe mass extinction. The combined input of carbon to the atmosphere from volcanic CO_2 degassing and mass mortality (and induced disequilibrium of the organic subcycle) leads to extremely high levels of atmospheric CO_2 and dissolved CO_2 in the deep ocean. Temperature-dependent weathering processes would have been strongly enhanced. The reduced primary productivity induces a drop in global organic carbon burial and a subsequent imbalance in the rates of deposition and weathering of sedimentary organic matter. The combination of the volcanic degassing and the ecosystem collapse is able to provide enough isotopically light carbon to bring about the drop in $\delta^{13}C$ at the PT boundary without invoking methane emission from the sediments. Multiple $\delta^{13}C$ pulses are not reproduced by the model simulations, but this could be a consequence of multiple inputs of volcanic CO_2 degassing or of multiple episodes of reduced marine productivity. However, the model only partly reproduces the complex variations of the $\delta^{13}C$ values occurring at the PT boundary [13]. A transient increase in $\delta^{13}C$ following the initial negative excursion is induced by the enhanced organic carbon burial during the productivity bloom and associated anoxia. The longer the Strangelove Ocean persists, the greater is the magnitude of the negative $\delta^{13}C$ excursion, and the shorter and more intense is the recovery phase and interval of deep anoxia.

Acknowledgements

This study has been financially supported by the French ECLIPSE program and a research grant ('Crédit aux chercheurs' 1.5.035.03, exercice 2002–2003) from the Belgian National Foundation for Scientific Research (FNRS). Partial support was also provided through a scientific cooperation between France and the Wallonie-Bruxelles Community of Belgium ("Tournesol" project). L.M.F. is Research Associate at FNRS. We thank P. Wignall and J. Veizer for their very constructive reviews, as well as G. Halverson for his very careful reading which strongly improved the final version of this manuscript.

References

[1] V. Courtillot, C. Jaupart, I. Manighetti, P. Tapponnier, J. Besse, On causal links between flood basalts and continental breakup, Earth Planet. Sci. Lett. 166 (1999) 177–195.

[2] D.M. Kerrick, Present and past nonanthropogenic CO_2 degassing from the solid earth, Rev. Geophys. 39 (4) (2001) 565–585.

[3] V.V. Zolotukhin, A.I. Al'Mukhamedov, Traps of the Siberian platform, in: J.D. Macdougall (Ed.), Continental Flood Basalts, Kluwer Academic Publishing, Amsterdam, 1988, pp. 273–310.

[4] M. Sharma, Siberian traps, in: J.J. Mahoney, M.F. Coffin (Eds.), Large Igneous Provinces: Continental, Oceanic, and Planetary Flood Volcanism, AGU Monograph, vol. 100, 1997, pp. 273–295.

[5] M.K. Reichow, A.D. Saunders, R.V. White, M.S. Pringle, A.I. Al'Mukhamedov, A.I. Medvedev, N.P. Kirda, $^{40}Ar/^{39}Ar$ dates from the West Siberian Basin: Siberian flood basalt province doubled, Science 296 (2002) 1846–1849.

[6] J.C. Claoué-Long, Z. Zhang, S. Du, The age of the Permian–Triassic boundary, Earth Planet. Sci. Lett. 105 (1991) 182–190.

[7] P.R. Renne, Z. Zichao, M.A. Richards, M.T. Black, A.R. Basu, Synchrony and causal relations between Permian–Triassic boundary crises and Siberian flood volcanism, Science 269 (1995) 1413–1416.

[8] S.A. Bowring, D.H. Erwin, Y. Jin, M.W. Martin, K. Davidek, W. Wang, U/Pb zircon geochronology and tempo of the end-Permian mass extinction, Science 280 (1998) 1039–1045.

[9] R. Mundil, I. Metcalfe, K.R. Ludwig, P.R. Renne, F. Oberli, R.S. Nicoll, Timing of the Permian–Triassic biotic crisis; implications from new zircon U/Pb age data (and their limitations), Earth Planet. Sci. Lett. 187 (2001) 131–145.

[10] I.H. Campbell, G.K. Czamanske, V.A. Fedorenko, R.I. Hill, V. Stepanov, Synchronism of the Siberian traps and the Permian–Triassic boundary, Science 258 (1992) 1760–1763.

[11] R.V. White, Earth's biggest 'whodunnit': unravelling the clues in the case of the end-Permian mass extinction, Philos. Trans. R. Soc. Lond., A 360 (2002) 2963–2985.

[12] R.A. Berner, Examination of hypotheses for the Permo-Triassic boundary extinction by carbon cycle modeling, Proc. Natl. Acad. Sci. 99 (2002) 4172–4177.

[13] Y.G. Jin, Y. Wang, W. Wang, Q.H. Shang, C.Q. Cao, D.H. Erwin, Pattern of marine mass extinction near the Permian–Triassic boundary in South China, Science 289 (2000) 432–436.
[14] W.T. Holser, H.-P. Schönlaub, M. Attrep Jr., K. Boeckelmann, P. Klein, M. Magaritz, C.J. Orth, A. Fenninger, C. Jenny, M. Kralik, H. Mauritsch, E. Pak, J.-M. Schramm, K. Stattegger, R. Schmöller, A unique geochemical record at the Permian/Triassic boundary, Nature 337 (1989) 39–44.
[15] P.B. Wignall, R. Morante, R. Newton, The Permo-Triassic transition in Spitsbergen: $\delta^{13}C_{org.}$ chemostratigraphy, Fe and S geochemistry, facies, fauna and trace fossils, Geol. Mag. 135 (1998) 47–62.
[16] A. Baud, M. Magaritz, W.T. Holser, Permian–Triassic of the Tethys: carbon isotope studies, Geol. Rundsch. 78 (1989) 649–677.
[17] W.T. Holser, M. Magaritz, Cretaceous/Tertiary and Permian/Triassic boundary events compared, Geochim. Cosmochim. Acta 56 (1992) 3297–3309.
[18] A. Hallam, P.B. Wignall, Mass Extinctions and their Aftermath, Oxford University Press, 1997, 330 pp.
[19] R.J. Twitchett, C.V. Looy, R. Morante, H. Visscher, P.B. Wignall, Rapid and synchronous collapse of marine and terrestrial ecosystems during the end-Permian biotic crisis, Geology 29 (2001) 351–354.
[20] P.B. Wignall, A. Hallam, Anoxia as a cause of the Permian/Triassic extinction: facies evidence from northern Italy and the western United States, Palaeogeogr. Palaeoclimatol. Palaeoecol. 93 (1992) 21–46.
[21] Y. Isozaki, Superanoxia across the Permo-Triassic boundary: record in accreted deep-sea pelagic chert in Japan, Can. Soc. Pet. Geol., Mem. 17 (1994) 805–812.
[22] P.B. Wignall, R.J. Twitchett, Oceanic anoxia and the end Permian mass extinction, Science 272 (1996) 1155–1158.
[23] P.B. Wignall, Large igneous provinces and mass extinctions, Earth-Sci. Rev. 53 (2001) 1–33.
[24] J.C.G. Walker, P.B. Hays, J.F. Kasting, A negative feedback mechanism for the long-term stabilization of Earth's surface temperature, J. Geophys. Res. 86 (1981) 9776–9782.
[25] C. Dessert, B. Dupré, L.M. François, J. Schott, J. Gaillardet, G.J. Chakrapani, S. Bajpai, Erosion of Deccan Traps determined by river geochemistry: impact on the global climate and the $^{87}Sr/^{86}Sr$ ratio of seawater, Earth Planet. Sci. Lett. 188 (2001) 459–474.
[26] P.V. Brady, The effect of silicate weathering on global temperature and atmospheric CO_2, J. Geophys. Res. 96 (1991) 18101–18106.
[27] C. Dessert, B. Dupré, J. Gaillardet, L.M. François, C.J. Allègre, Basalt weathering laws and the impact of basalt weathering on the global carbon cycle, Chem. Geol. 202 (2003) 257–273.
[28] M. Javoy, G. Michard, EOS Trans. AGU 70 (1989) 1421.
[29] C.R. Scotese, Atlas of Earth History. 2001 Paleomap Progress Report 90-0497, Department of Geology, University of Texas, Arlington, TX, 2001.
[30] R.M. Hotinski, K.L. Bice, L.R. Kump, R.G. Najjar, M.A. Arthur, Ocean stagnation and end-Permian anoxia, Geology 29 (2001) 7–10.
[31] K. Faure, M. de Wit, J.P. Willis, Late Permian global coal hiatus linked to ^{13}C-depleted CO_2 flux into the atmosphere during the final consolidation of Pangea, Geology 23 (1995) 507–510.
[32] L.M. François, J.C.G. Walker, Modelling the Phanerozoic carbon cycle and climate: constraints from the $^{87}Sr/^{86}Sr$ isotopic ratio of seawater, Am. J. Sci. 292 (1992) 81–135.
[33] J.T. Parrish, Latitudinal distribution of land and shelf and absorbed solar radiation during the Phanerozoic, United States of Geological Survey, Open-File Report 85–31 (1985) 21 pp.
[34] M.I. Budyko, The effect of solar radiation variations on the climate on the Earth, Tellus 21 (1969) 611–619.
[35] P.M. Rees, M.T. Gibbs, A.M. Ziegler, J.E. Kutzbach, P.J. Behling, Permian climates: evaluating model predictions using global paleobotanical data, Geology 27 (1999) 891–894.
[36] J. Gaillardet, B. Dupré, P. Louvat, C.J. Allègre, Global silicate weathering and CO_2 consumption rates deduced from the chemistry of the large rivers, Chem. Geol. 159 (1999) 3–30.
[37] M. New, M. Hulme, P.D. Jones, Representing twentieth-century space–time climate variability. Part II: development of 1901–1996 monthly grids of terrestrial surface climate, J. Climate 13 (2000) 2217–2238.
[38] R.A. Berner, Z. Kothavala, GEOCARB III: a revised model of atmospheric CO_2 over Phanerozoic time, Am. J. Sci. 301 (2001) 182–204.
[39] P.N. Froelich, M.L. Bender, N.A. Luedtke, G.R. Heath, T. DeVries, The marine phosphorus cycle, Am. J. Sci. 282 (1982) 474–511.
[40] T. Tyrrell, The relative influences of nitrogen and phosphorus on oceanic primary production, Nature 400 (1999) 525–531.
[41] Y. Goddéris, L.M. François, J. Veizer, The early Paleozoic carbon cycle, Earth Planet. Sci. Lett. 190 (2001) 181–196.
[42] K.H. Freeman, J.M. Hayes, Fractionation of carbon isotopes by phytoplankton and estimates of ancient CO_2 levels, Glob. Biogeochem. Cycles 6 (1992) 185–198.
[43] W.G. Mook, J.C. Bommerson, W.H. Staverman, Carbon isotope fractionation between dissolved bicarbonate and gaseous carbon dioxide, Earth Planet. Sci. Lett. 22 (1974) 169–176.
[44] C. Korte, H.W. Kozur, M.M. Joachimski, H. Strauss, J. Veizer, L. Schwark, Carbon, sulfur, oxygen and strontium isotope records, organic geochemistry and biostratigraphy across the Permian/Triassic boundary in Abadeh, Iran, Int. J. Earth Sci. 93 (2004) 565–581.
[45] Y. Kajiwara, S. Yamakita, K. Ishida, H. Ishiga, A. Imai, Development of a largely anoxic stratified ocean and its temporary massive mixing at the Permian/Triassic boundary supported by the sulfur isotopic record, Palaeogeogr. Palaeoclimatol. Palaeoecol. 111 (1994) 367–379.
[46] M. Gruszczynski, A. Hoffman, K. Malkowski, J. Veizer, Seawater strontium isotopic perturbation at the Permian–Triassic boundary, West Spitsbergen, and its implications for the interpretation of strontium isotopic data, Geology 20 (1992) 779–782.
[47] S.L. Kamo, G.K. Czamanske, Y. Amelin, V.A. Fedorenko, D.W. Davis, V.R. Trofimov, Rapid eruption of Siberian flood-volcanic rocks and evidence for coincidence with the

Permian–Triassic boundary and mass extinction at 251 Ma, Earth Planet. Sci. Lett. 214 (2003) 75–91.
[48] D.C. Engebretson, K.P. Kelley, H.J. Cashman, M.A. Richards, 180 million years of subduction, GSA Today 2 (1992) 93–95.
[49] S. Gaffin, Ridge volume dependence on seafloor generation rate and inversion using long term sealevel change, Am. J. Sci. 287 (1987) 596–611.
[50] A.J. Boucot, J. Gray, A critique of Phanerozoic climatic models involving changes in the CO_2 content of the atmosphere, Earth-Sci. Rev. 56 (2001) 1–159.
[51] P. Van Cappellen, E.D. Ingall, Redox stabilization of the atmosphere and oceans by phosphorus-limited marine productivity, Science 271 (1996) 493–496.
[52] L.R. Kump, Interpreting carbon-isotope excursions: strangelove oceans, Geology 19 (1991) 299–302.
[53] S. D'Hondt, P. Donaghay, J.C. Zachos, D. Luttenberg, M. Lindinger, Organic carbon fluxes and ecological recovery from the Cretaceous–Tertiary mass extinction, Science 282 (1998) 276–279.
[54] H.S. Mii, E.L. Grossman, T.E. Yancey, Stable carbon and oxygen isotope shifts in Permian seas of West Spitsbergen—global change or diagenetic artifact? Geology 25 (1997) 227–230.
[55] UNESCO, Geological World Atlas, UNESCO Press, Paris, 1976.
[56] P. Amiotte-Suchet, J.L. Probst, W. Ludwig, World wide distribution of continental rock lithology: implications for the atmospheric/soil CO_2 uptake by continental weathering and alkalinity river transport to the oceans, Glob. Biogeochem. Cycles 17 (2003). doi:10.1029/2002GB001891 (electronic version).
[57] J.G. Souther, R.L. Armstrong, J. Harakal, Chronology of the peralkaline, late Cenozoic Mount Edziza volcanic complex, northern British Columbia, Canada, Geol. Soc. Amer. Bull. 95 (1984) 337–349.
[58] M.T. Mangan, T.L. Wright, D.A. Swanson, G.R. Byerly, Regional correlation of Grande Ronde Basalt flows, Columbia River Basalt Group, Washington, Oregon, and Idaho, Geol. Soc. Amer. Bull. 97 (1986) 1300–1318.
[59] T.J. Crowley, W.T. Hyde, D.A. Short, Seasonal cycle variations on the supercontinent of Pangea, Geology 17 (1989) 457–460.
[60] W.S. Broecker, S. Peacock, An ecologic explanation for the Permo-Triassic carbon and sulfur isotope shifts, Glob. Biogeochem. Cycles 13 (1999) 1167–1172.
[61] D.J. Beerling, R.A. Berner, Biogeochemical constraints on the Triassic–Jurassic boundary carbon cycle event, Glob. Biogeochem. Cycles 16 (2002) 101–113.